Device

Article

Deep-learning-enhanced metal-organic framework e-skin for health monitoring

Graphical abstract

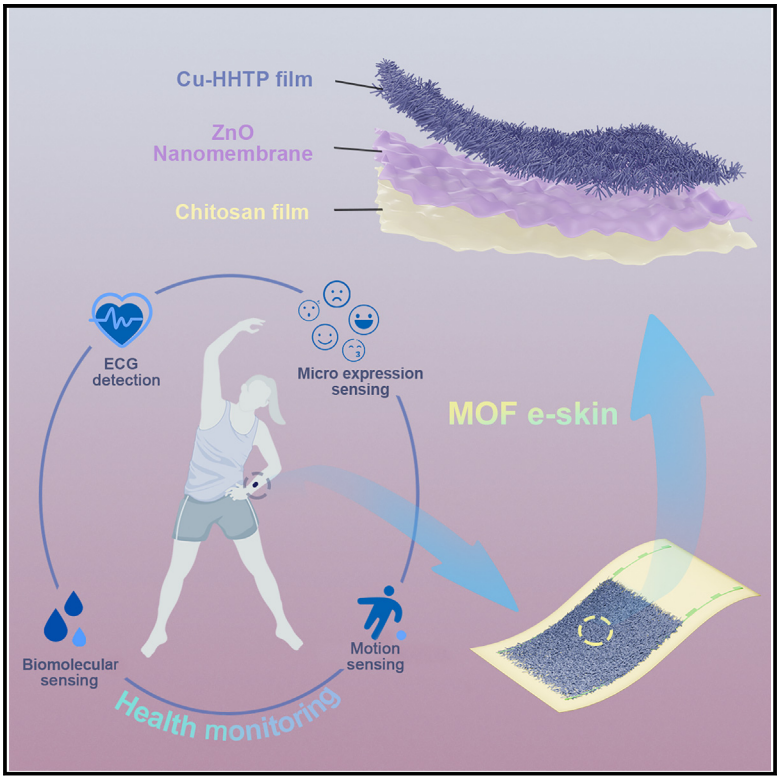

Highlights

- MOF e-skin for motion detection and biomolecular sensing
- Mechanisms of biomolecular and motion sensing are investigated
- Integration of deep learning helps to distinguish the micro-expressions
- Atomic-layer deposition provides an efficient approach to fabricate sensor array

Authors

Xinyi Ke (柯昕逸), Yifan Duan (段逸凡), Yifei Duan (段逸非), ..., Yongfeng Mei (梅永丰), Gaoshan Huang (黄高山), Junhao Chu (褚君浩)

Correspondence

zhezhao@dhu.edu.cn (Z.Z.), gshuang@fudan.edu.cn (G.H.)

In brief

The multi-functional e-skin composed of self-locking chitosan film and conductive metal-organic framework film is designed and fabricated to integrate the detection of multiple physiological signals, including lactic acid, glucose, and motion. The utilization of the transformer neural network in data analyses achieves precise recognition of the signal and meanwhile differentiation of multiple stimuli is realized. This approach represents a significant leap in e-skin technology, enhancing its capability for comprehensive health monitoring.

Ke et al., 2025, Device *3*, 100650
April 18, 2025
https://doi.org/10.1016/j.device.2024.100650

CellPress

Develop
Prototype with demonstrated applications in relevant environment

Please cite this article in press as: Ke et al., Deep-learning-enhanced metal-organic framework e-skin for health monitoring, Device (2024), https://doi.org/10.1016/j.device.2024.100650

Device

CellPress
OPEN ACCESS

Article

Deep-learning-enhanced metal-organic framework e-skin for health monitoring

Xinyi Ke (柯昕逸),[1,3,4] Yifan Duan (段逸凡),[5] Yifei Duan (段逸非),[6] Zhe Zhao (赵哲),[2,*] Chunyu You (尤淳瑜),[1] Tingting Sun (孙婷婷),[2] Xingyu Gao (高兴宇),[2] Ziyu Zhang (张子煜),[1] Wen Xue (薛雯),[2] Xuanyong Liu (刘宣勇),[2] Yongfeng Mei (梅永丰),[1,3,4] Gaoshan Huang (黄高山),[1,4,7,*] and Junhao Chu (褚君浩)[1,3]

[1]Department of Materials Science, International Institute for Intelligent Nanorobots and Nanosystems, State Key Laboratory of Surface Physics, and State Key Laboratory of Photovoltaic Science and Technology, Fudan University, Shanghai 200433, P.R. China

[2]State Key Laboratory for Modification of Chemical Fibers and Polymer Materials, College of Biological Science and Medical Engineering, Donghua University, Shanghai 201620, P.R. China

[3]Shanghai Frontiers Science Research Base of Intelligent Optoelectronics and Perception, Institute of Optoelectronics, Fudan University, Shanghai 200433, P.R. China

[4]Yiwu Research Institute of Fudan University, Yiwu, Zhejiang 322000, P.R. China

[5]Department of Materials Science and Engineering, University of California, Berkeley, Berkeley, CA 94720-1760, USA

[6]Department of Materials Science and Engineering, University of Pennsylvania, Philadelphia, PA 19104, USA

[7]Lead contact

*Correspondence: zhezhao@dhu.edu.cn (Z.Z.), gshuang@fudan.edu.cn (G.H.)

https://doi.org/10.1016/j.device.2024.100650

THE BIGGER PICTURE Multi-functional e-skin replicates the tactile and sensory functions of human skin, providing enhanced sensitivity and adaptability compared to conventional sensors. This makes it valuable for applications in healthcare monitoring, prosthetics, and human-machine interfaces. However, fabrication of e-skin capable of achieving different sensing abilities is challenging. Previous approaches involve the engagement of diverse sensing materials, but this leads to complex and costly fabrication process, and many devices fail to demonstrate high performance. In addition, difficulty exists in signal differentiation, particularly for simultaneous detecting multiple stimuli. Here, a high-performance multi-functional metal-organic framework (MOF) film-based e-skin on chitosan film that integrates the detection abilities of biomolecules, motion, electrocardiogram, etc. is prepared, and precise signal differentiation is achieved by adopting deep learning, using transformer neural networks in data analyses.

SUMMARY

Electronic skin (e-skin) mimics the sensing abilities of human skin and offers sensitivity and flexibility, which has garnered attention for medical health monitoring. Nonetheless, limitations in the properties of active materials and signal-to-noise ratio hinder the implementation of multi-functional detection such as integrating biomolecular sensing, motion detection, and electrocardiography in a single device. Here, we introduce a strategy of preparing a multi-functional e-skin that utilizes a composite material combining self-locking chitosan and conductive metal-organic framework film, achieving high-performance motion detection and biomolecular sensing. The integration of deep learning, specifically transformer neural networks, aids in recognizing subtle facial micro-expressions. A sensing array is crafted by utilizing a rapid assembly method that supports discerning more attributes with heightened precision.

INTRODUCTION

Electronic skin (e-skin) has emerged as a transformative technology capable of sensing both physiological (internal) and environmental (external) stimuli analogous to human skin.[1,2] In particular, multi-functional e-skin can mimic the tactile and sensory capabilities of human skin, providing remarkable sensitivity and versatility.[3–6] E-skin has recently been evolved in terms of device dimensions, functionalities, and stability, making it suitable for practical applications in diverse fields,[7–16] including robotics, sports science, and healthcare. Moreover, researchers have recently been focused on potential applications of e-skin in biomarker detection[17,18] and human mechanosensation.[5,19] The selection of sensing active materials is of importance for e-skin, and it is challenging to design a high-performance e-skin capable of sensing different stimuli within one individual device. The identification of signals from multi-functional e-skin is also difficult.[20] The prevalent approach to producing multi-functional e-skin

Please cite this article in press as: Ke et al., Deep-learning-enhanced metal-organic framework e-skin for health monitoring, Device (2024), https://doi.org/10.1016/j.device.2024.100650

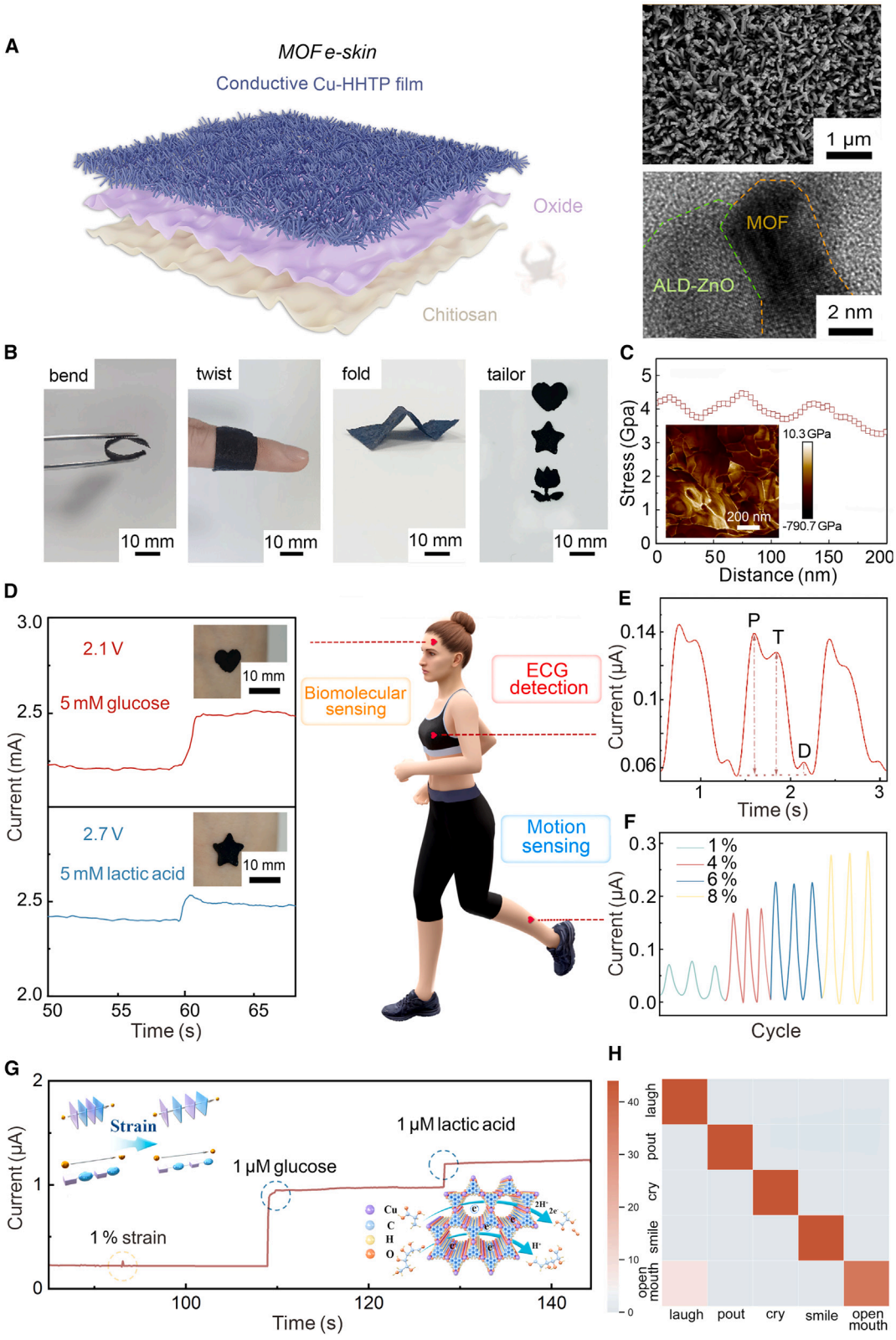

(legend on next page)

Please cite this article in press as: Ke et al., Deep-learning-enhanced metal-organic framework e-skin for health monitoring, Device (2024), https://doi.org/10.1016/j.device.2024.100650

involves the integration of diverse sensing materials; however, this method is often associated with complex and costly fabrication processes, and many of these materials fail to demonstrate high performance.[21,22] Most of the substrates are conventional elastomers (e.g., polydimethylsiloxane [PDMS], Ecoflex),[22] while the elastomers lack permeability to air and sweat vapor, which will lead to skin irritation during body sensing and affect the signal due to sweat accumulation.[23] As for active material, conductive metal-organic frameworks (MOFs) have emerged as a promising alternative due to their unique properties, including electrochemical properties, open-access pore structures, and high customizability,[7,24] Nonetheless, the advancement of MOFs is impeded by challenges in fabricating stable and continuous MOF films with designed microstructures. The synthesis of MOF films typically relies on methods such as drop casting the MOF dispersion solution, which tends to dilute the concentration of MOFs and reduce the active surface area. Adhesion between active film and substrate becomes a concern.[25–27] Alternatively, the electrodeposition method is often employed, but it is more complex and costly.[28]

In this work, a multi-functional MOF film-based e-skin that integrates the detection of physiological signals such as lactic acid (LA), glucose (GL), motion, and electrocardiogram (ECG) is prepared. Conductive MOF (Cu-2,3,6,7,10,11-hexahydroxytriphenylene [HHTP]) film is prepared on a chitosan substrate using the induction effect of pre-deposited oxide nanomembranes via atomic-layer deposition (ALD),[29] achieving adhesion, uniformity, and conformality. In the composite, Cu-HHTP enhances the conductivity and sensitivity of the e-skin for health monitoring, with machine learning aiding in micro-expression detection. Additionally, Cu-HHTP demonstrates biosensing performance for LA and GL, offering high sensitivity, low detection limits, and broad linear ranges. The mechanisms of both sensing models have been studied, and the results indicate that the alterations in the carrier transfer path and the redox reactions facilitate motion detection and biomolecular sensing, respectively. In particular, the active sites of MOF film during biosensing are investigated, elucidating the outstanding biomolecular sensing performance.

RESULTS AND DISCUSSION

Fabrication and characterization of MOF e-skin for multi-functional sensing

To fabricate MOF e-skin, a self-locking chitosan film is first achieved from crab shells by several steps and then conductive Cu-HHTP film is conformally grown on the chitosan film (Note S1; Figures S1–S3). The schematic diagram in Figure 1A presents an overview of the composite sample structure, with the left inset displaying the scanning electron microscope (SEM) image of Cu-HHTP on the substrate. SEM image and the corresponding energy dispersive spectroscopy (EDS) mapping results in Figure S4 illustrate the conformable growth of Cu-HHTP film on chitosan film. The high C, N, O, Zn, and Cu concentrations confirm the existence of MOF film, while the ZnO nanomembrane as the induction layer negligibly exists (Figures S5). Additionally, from the transmission electron microscopy (TEM) images in Figure S6 (larger magnification) and the right insets of Figure 1A (lower magnification), it is evident that Cu-HHTP grows tightly on the substrate, facilitated by the presence of the ZnO nanomembrane with induction effect.[30] As an advanced e-skin, the fabricated sample exhibits flexibility and customizability, enabling adaptive interfacial properties to human skin, depicted in Figure 1B. In addition, the size of MOF particles is ~200 nm, while the MOF film exhibits a roughness smaller than the particle size (Figure S7), implying a smooth and uniform structure for enhanced sensing performance.[29] It is worth noting that the dual-sided nature of the current MOF e-skin (Note S2; Figure S8) substantially augments its biosensing capabilities.[31]

The mechanical properties of the e-skin are studied. Figure 1C shows a typical stress-distance curve of MOF e-skin. Corresponding elastic moduli map of MOF e-skin calculated from the Derjaguin, Muller, and Toporov (DMT) model is shown in the inset of Figures 1C,[24] which is in the order of GPa. The simulated strain and stress curve of MOF e-skin with a curvature radius of 10 mm is plotted in Figure S9, and a linear strain-stress plot can be observed. However, a break is noticeable due to the different elastic moduli of MOF film and chitosan film. Here, the maximum strain in the MOF film is less than 5%, and the integrity of the e-skin under such deformation can be proved by additional stretching test (Figure S10). The reproducibility and mechanical property under different relative humidities (Figure S11) lay a foundation for the practical application of MOF e-skin.[32] More detailed structural characterizations of MOF e-skin can be found in Note S3 and Figures S12–S15. When functioning as a biosensor and being adhered to the forehead, the MOF e-skin can detect LA and GL at different voltages because unstable sites within the MOF facilitate redox reactions (Figure 1D). As a motion sensor, when placed around the thorax, the MOF e-skin can be used as an ECG sensor, recording pulse waves, i.e., percussion peaks (P), tidal peaks (T), and diastolic peaks (D) (Figure 1E).[33] Furthermore, variations in the strain of the e-skin can be identified based on the output current (Figure 1F). More importantly, we can verify these three stimuli by the amplitude of the output current, as the current response from the strain is much smaller compared with those from biomolecules

Figure 1. Fabrication and performance of MOF e-skin

(A) Overview of the fabrication process of MOF e-skin. Lower left inset is the SEM image of MOF e-skin. Right insets are TEM images with different magnitudes.

(B) Flexibility and designability of synthesized MOF e-skin.

(C) The stress-distance curve of MOF e-skin. Inset is the atomic force microscopy (AFM) image obtained from the DMT model.

(D) I-t curves of biosensing results of MOF e-skin. Top: I-t curve of MOF e-skin with 5 mM GL added at 2.1 V. Bottom: I-t curve of MOF e-skin with 5 mM LA added at 2.7 V.

(E) I-t curve of MOF e-skin for ECG detection. P, percussion wave; T, tidal wave; D, diastolic wave.

(F) I-t curve of MOF e-skin with different strains applied.

(G) I-t curve of MOF e-skin with 1% strain, 1 μM GL, and 1 μM LA applied sequentially. Insets demonstrate corresponding sensing mechanisms.

(H) Confusion matrix for the recognition of five types of micro-expressions of the transformer neural network for the test dataset.

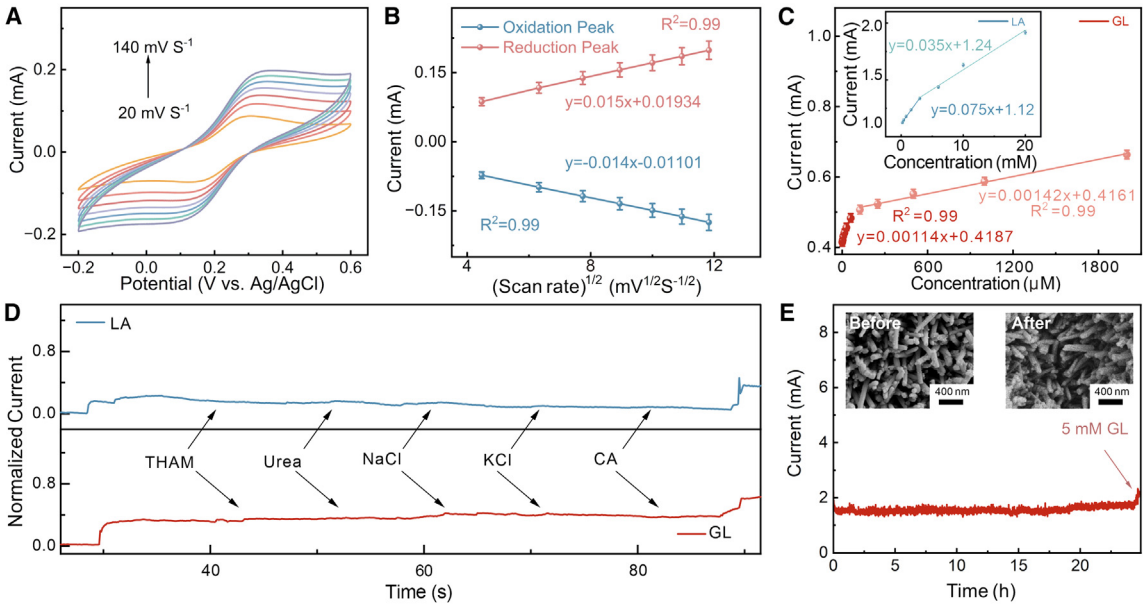

Figure 2. Biosensing performance and mechanism of the MOF e-skin

(A) CV scans of MOF e-skin at diverse scan rates.

(B) The oxidation peak current and the reduction peak current plotted as functions of the square root of the scan rate, derived from (A), where error bars indicate standard deviation.

(C) Calibration plot of GL sensing. Inset is calibration plot of LA sensing. The error bars indicate standard deviation.

(D) I-t curve of the MOF e-skin for the continuous addition of 1.0 mM GL/LA and 0.1 mM of various interferents at applied potentials of 2.1 (lower panel) and 2.7 V (upper panel).

(E) I-t curve of the MOF e-skin in 0.1 M PBS with 5.0 mM GL at 2.1 V. 5 mM GL is added to the solution after 24 h to test the performance recovery. Inset is the SEM images of MOF e-skin before and after continuous sensing test of 24 h.

(Figure 1G). The proposed mechanisms underlying the sensor's operation are illustrated in the insets of Figure 1G. For a conductive MOF, carrier transfer occurs via two primary methods: through-bond or through-space.[34,35] When tensile strain is applied to the MOF e-skin, the previously disordered pathway is aligned and integrated to create a conductive highway for electron transportation, leading to an increased current. Biomolecular sensing, on the other hand, relies on the redox reaction between biomolecules and active sites. In this context, a hydrogen atom from GL (LA) is transferred to *OH via an electron-proton-coupled transfer process, resulting in the formation of $*H_2O$.[7] This reaction exposes the free active sites of Cu-HHTP and facilitates the desorption of H_2O, which benefits the redox reaction and causes the increased current.[30,36]

Using transformer neural network for micro-expression recognition

We have adopted the neural network to assist in analyzing the output data of the e-skin. The transformer, a deep-learning model known for its ability to capture complex dependencies in sequential data,[37] is applied to processing signal sequences and it enhances the recognition accuracy of complex motion patterns. As demonstrated in Figure 1H, our system identifies various micro-expressions with high prediction accuracy. Here, the y axis represents the actual expression, while the x axis displays the predicted expression. We can differentiate between pout, cry, and smile. However, a few laugh expressions are mistakenly predicted as open mouth due to similar facial movements. This underscores the pattern recognition capabilities of e-skin. In addition, we notice that deep-learning technology can help to decouple the e-skin's responses from motion and biomolecules (Figure S16).

Application demonstrations

Biomolecular sensing tested with MOF e-skin

On the basis of biocompatibility and breathability (Note S4; Figures S17–S19), MOF e-skin is used as biomolecular sensors for both GL and LA. To quantitatively assess the electrochemical activity of the MOF e-skin, the active area of the composites was evaluated by using $K_3[Fe(CN)_6]$ as an electrochemical probe.[38,39] The cyclic voltammetry (CV) scans of the MOF e-skin, depicted in Figure 2A, exhibit both oxidation and reduction peaks across different scan rates. Notably, as the scan rate increases from 20 to 140 mV s^{-1}, the peak currents for both oxidation and reduction rise correspondingly. The active area (A) of the electrode materials can be calculated by using the Randles-Sevcik equation:[30]

$$I_{peak} = (2.69 \times 10^5) n^{3/2} A D^{1/2} C v^{1/2},$$

where *n* represents the number of transferred electrons, and D and C denote the diffusion coefficient and the bulk concentration of $K_3[Fe(CN)_6]$, respectively. According to the slope of the peak current versus the square root of the scan rate (Figure 2B), the calculated A for the MOF e-skin is 0.133 cm^2. This active area

Please cite this article in press as: Ke et al., Deep-learning-enhanced metal-organic framework e-skin for health monitoring, Device (2024), https://doi.org/10.1016/j.device.2024.100650

enhances the contact between electrode and active species in the electrolyte and facilitates interfacial electron transfer, thereby improving the electrochemical performance of the MOF e-skin.[40] Subsequently, the sensing ability of MOF e-skin toward GL and LA are examined (Note S5; Figures S20–S23), and the derived calibration plots are shown in Figure 2C. The inset of Figure 2C demonstrates an ultrahigh GL sensitivity of 11,480 μA mM^{-1} cm^{-2} and a wide linear range of 0.001–2 mM (linear regression equation, Y = 0.00142X+0.4161; correlation coefficient, R^2 = 0.99). With the larger concentration of GL, the linear range can be extended to 20 mM, with a linear regression equation Y = 0.0419X+2.141, R^2 = 0.99 (Figure S24). Furthermore, the limit of detection (LOD) of GL is calculated by using the equation LOD = 3δ/S, where δ is the standard deviation and S is the sensitivity, and thus an LOD of 0.335 μM is obtained. Here, first-principles calculations based on periodic density functional theory (DFT) were used to analyze the sensing mechanism of the GL biosensor, and detailed model structures and calculations are shown in Note S5 and Figures S25–S28.

For assessing the performance of the sensor, the anti-interference capability is critical. The upper panel of Figure 2D illustrates the I-t curve of the MOF e-skin upon the sequential addition of 1 mM GL, followed by 0.1 mM of various interferents, including tromethamine (THAM), urea, NaCl, KCl, and citric acid (CA), and concluding with an additional 1.0 mM GL. The results highlight that these interferents elicit a minimal current response when compared to GL, thereby demonstrating the sensor's anti-interference capability. Given that LA operates within the same interference milieu as GL, its resistance to the same set of interferents is tested, affirming comparable anti-interference efficacy (lower part of Figure 2D). Long-term stability is a critical attribute for sensors. In this work, the long-term performance of the MOF e-skin is assessed at 2.1 V in 0.1 M PBS containing 5 mM GL. As depicted in Figure 2E, the current response remains stable over a 24-h period without noticeable deterioration, indicating the MOF e-skin's long-term stability. Because of its recovery capability, the MOF e-skin continues to exhibit a current response to 5 mM GL even after 24 h of evaluation. The insets of Figure 2E, which display the morphologies of the MOF e-skin before and after a 24-h sensing test, reveal no discernible changes, further showing its remarkable stability. With the same method, the LA sensor shows an outstanding stability and recovery capability within 24 h (Figure S29). Furthermore, the reproducibility of the sensor was assessed by detecting 1 mM GL with the same sensor on five separate occasions, and the sensor was thoroughly washed in water after each test. As illustrated in Figure S30, the consistency of the response current, shown by a relative standard deviation (RSD) of 1.35%, attests to the sensor's reproducibility. This is attributed to the efficient adsorption-desorption process for GL molecules.[32] When compared to other MOF-based GL sensors, the MOF e-skin exhibits improved performance in terms of linear range, sensitivity, stability, RSD, and LOD, as summarized in Figure S31.[41–45]

Motion sensing tested with MOF e-skin

To explore the motion-sensing capabilities of the MOF e-skin, a series of measurements were conducted, encompassing bending, stretching, and other evaluations, with the results presented in Figure 3. Figure 3A demonstrates the bending status of the MOF e-skin as it conforms to tubes of varying diameters (Figure S32). A decrease in tube diameter indicates an increased degree of bending and results in a larger stretching in MOF e-skin and an increase in current (as detailed in the inset of Figure 3A). The calibration curve for bending sensitivity is described by the equation Y = 0.0488 + 0.076X, R^2 = 0.99. Additionally, the corresponding calibration curve for stretching sensing is represented by the equation Y = 0.2711 − 0.2303X, R^2 = 0.99 (Figure 3B). The long-term stability of the MOF e-skin was assessed through a series of loading/unloading tests extending over more than 800 cycles at a maximum strain of 4%. The MOF e-skin exhibits negligible variation throughout the testing period, as illustrated in Figure 3C. Here, the highest current response in each panel is normalized to 1 for comparison. The left and right insets of Figure 3C display the current variations of the sensor from 83 to 286 s (left) and from 673 to 676 s (right), respectively. The consistency of the observed curves indicates the suitability of the MOF e-skin for potential applications. Figure 3D presents an amplifying I-t curve of the MOF e-skin with a quick pressure stimulus where response time of ∼80 ms was measured (Figure S33). In addition, a designed pattern of the e-skin can be adhered to the human throat to distinguish various spoken words. As demonstrated in Figure 3E, the utterance of the word "hello" with increasing volumes results in a distinctive I-t curve characterized by an increased current. Similarly, other words such as "Fudan" and "morning" result in specific current responses, as illustrated in Figures S34A and S34B. Notably, even for actions such as swallowing (Figure S34C), the MOF e-skin consistently provides repeatable and prompt responses. Furthermore, MOF e-skin presents an outstanding ability to detect micro-expression. As shown in Figures 3F and S34D, when MOF e-skin is stuck near the mouth and eyes, clear current responses can be observed when micro-expressions appear.

Micro-expression recognition tasks of MOF e-skin

We conducted data analysis and processing by using the transformer neural network architecture on the sensing signals of micro-expressions (Figure 4A; Note S6). Our task predicts various expressions (cry, laugh, smile, pout, and open mouth) from electric current waveform graphs, framed as a sequential signal classification problem (Figure 4B). The transformer architecture is selected for its ability to capture features across long sequences.[37] We built a transformer-based model using Pytorch, adapting the similar coding of the vision transformer (ViT).[46] The model processes these signal embeddings through several layers of transformer blocks within the neural network architecture, with each block containing self-attention and feedforward neural networks, outputting probabilities for each category via a classification head. Due to the high manual signal collection costs, we employed displacement and noise addition for data augmentation. For instance, the data in Figure 4C have been augmented through shifting horizontally along the time axis. More displacement examples are shown in Figure S35A, and methods combining noise addition and displacement are shown in Figure S35B. Signal trimming is applied to remove noise from device startup and shutdown. The trimmed micro-expression signal examples can be observed in Figure 4D. These methods

Please cite this article in press as: Ke et al., Deep-learning-enhanced metal-organic framework e-skin for health monitoring, Device (2024), https://doi.org/10.1016/j.device.2024.100650

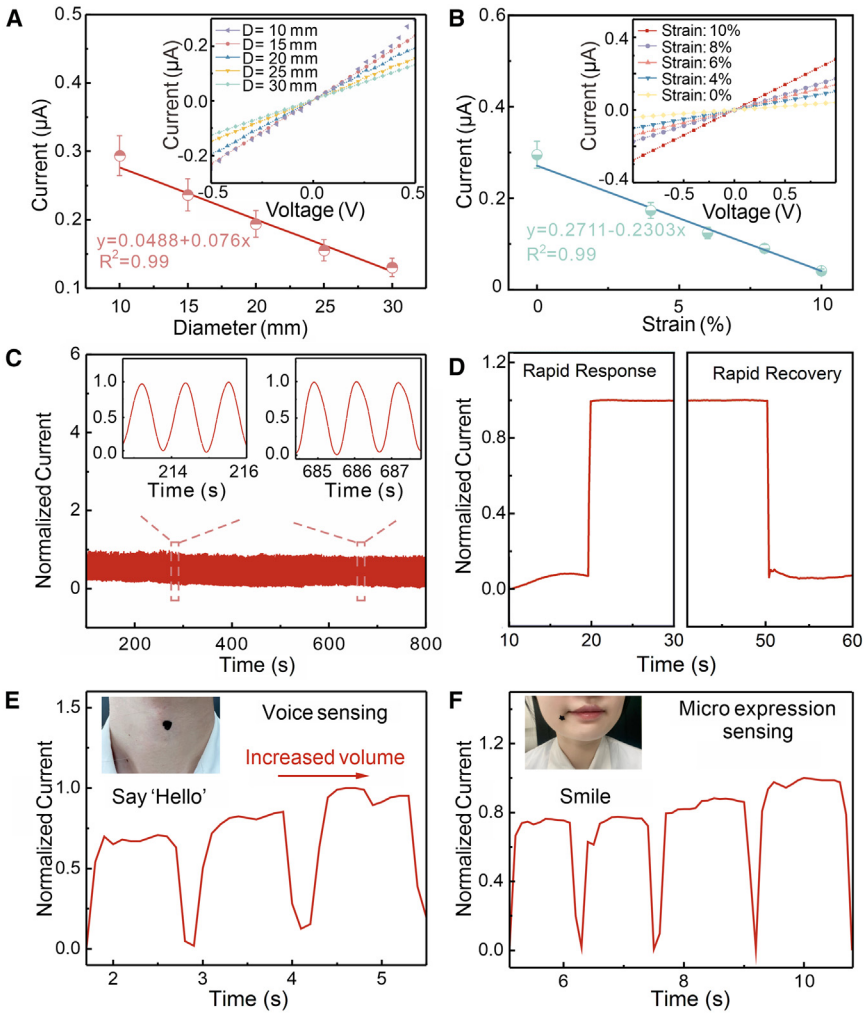

Figure 3. The motion-sensing performance of the MOF e-skin

(A) Current as a function of bending diameter, derived from inset. Inset: I-V curve of e-skin bent with different diameters, where error bars indicate standard deviation.

(B) Current-stretching strain curve, derived from inset. Inset: I-V curve of e-skin stretched with different strains, where error bars indicate standard deviation.

(C) The current variation of the MOF e-skin for 800 cycles of loading (4% strain)-unloading cycles. The insets show enlarged plots in the ranges of 283–286 s (left) and 673–676 s (right).

(D) Relative current variation of the MOF e-skin under a sudden strain stimulus, demonstrating rapid response (left) and recovery (right).

(E) The relative current variation of the MOF e-skin stuck on the throat of a volunteer, who says "Hello" three times.

(F) The relative current variation of the MOF e-skin stuck near the mouth of the volunteer, who smiles five times.

are suitable for micro-expression signals because temporal shifts do not compromise the accuracy of micro-expression information, and the addition of noise enhances network generalization across various environments. The test history in Figures 4E and 4F elucidate that the model achieves high accuracy and low training errors after 1,000 rounds, and the training-set learning curves and the confusion matrices are shown in detail in Figures S36 and S37. The model performance presented in a confusion matrix (Figure 1H) indicates micro-expression classification. To illustrate the practical application of the current approach, a demonstration of the sensing and recognition process is presented in Figure S38.

Transferred MOF e-skin array

To advance the study of MOF e-skin integration with transformer neural networks, incorporating an array is recommended, as an extensive array can enhance the ability to detect a wider range of physical properties from objects with greater precision. In the experiment, in order to transfer MOF film to target substrate for fabrication transferred e-skin array, we devised a multi-layered structure to facilitate the detachment of the MOF film from the original substrate. The design incorporates three additional layers before the assembly of MOF film,[29] as depicted in Figure 5A. The foundational layer, positioned at the base, functions as a sacrificial layer capable of withstanding high temperatures and severe chemical conditions, and it can be readily removed to liberate the overlying film. The subsequent layer, the interfacial layer, remains chemically inert throughout the fabrication process, facilitating the preservation of the integrity of the MOF film. The third layer, which is the induction layer, participates in the MOF film formation process. Here, poly(3,4-ethylenedioxythiophene)/poly(styrenesulfonate) (PEDOT/PSS) layer, ALD Al_2O_3 nanomembrane, and ALD-ZnO nanomembrane are used as sacrificial layer, interfacial layer, and induction layer, respectively.[29] The optical microscopy image of the multi-layered structure is exhibited in the inset of Figure 5A, and the obtained free-standing Cu-HHTP film via this approach is shown in Figure S39 with the large lateral size. The SEM image in Figure 5B demonstrates the dense and uniform structure of the free-standing MOF film, with the inset providing a magnified view. Figure 5C depicts the design of MOF e-skin array prepared by a transferring process and a top view of a single enlarged MOF e-skin unit is shown in the inset. Upon transfer onto a chitosan film substrate, a transferred MOF e-skin is achieved (Figure 5D). It is evident that the transferred MOF e-skin exhibits current response upon the addition of 5 mM LA in 0.1 M PBS at a potential of 2.7 V, as well as 5 mM GL in 0.1 M PBS at a potential of 2.1 V (Figure 5E). This response is slightly lower than that of the previous normal MOF e-skin, likely due to minor damage incurred during the transfer process. Additionally, subjecting the

Please cite this article in press as: Ke et al., Deep-learning-enhanced metal-organic framework e-skin for health monitoring, Device (2024), https://doi.org/10.1016/j.device.2024.100650

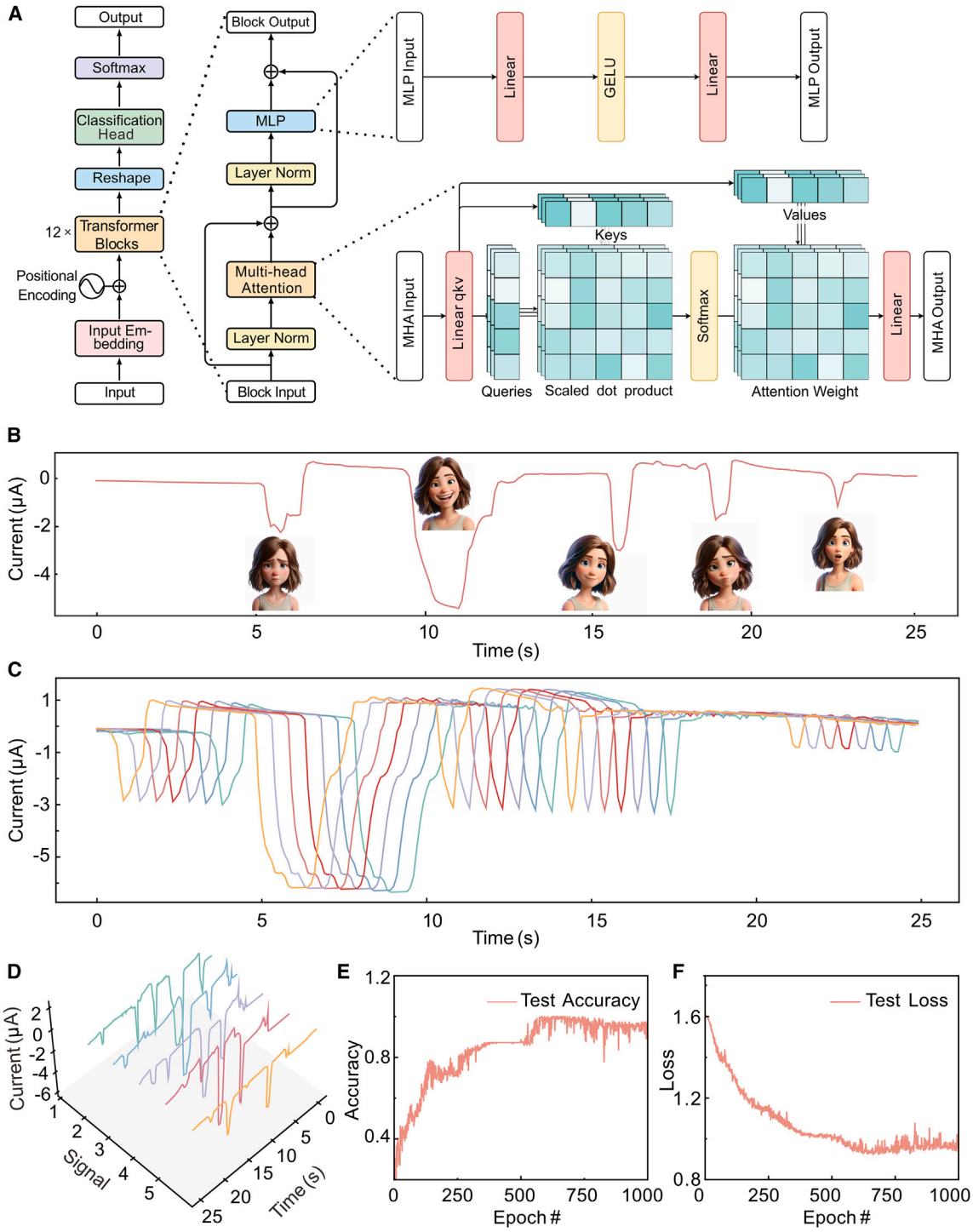

Figure 4. Applying transformer model in micro-expression analysis: From architecture to performance metrics

(A) Transformer model architecture for processing motion signals, with the multi-head attention, and multilayer perceptron module components.

(B) A signal triggered by five micro-expressions: cry, laugh, smile, pout, and open mouth.

(C) Data augmentation is employed to enhance the model's generalization capabilities.

(D) Five sets of examples of micro-expression signals, with each set consisting of a unique micro-expression depicted in (B).

(E and F) The learning progression of the model across the number of epochs: raising accuracy (E) and decreasing test loss (F).

Please cite this article in press as: Ke et al., Deep-learning-enhanced metal-organic framework e-skin for health monitoring, Device (2024), https://doi.org/10.1016/j.device.2024.100650

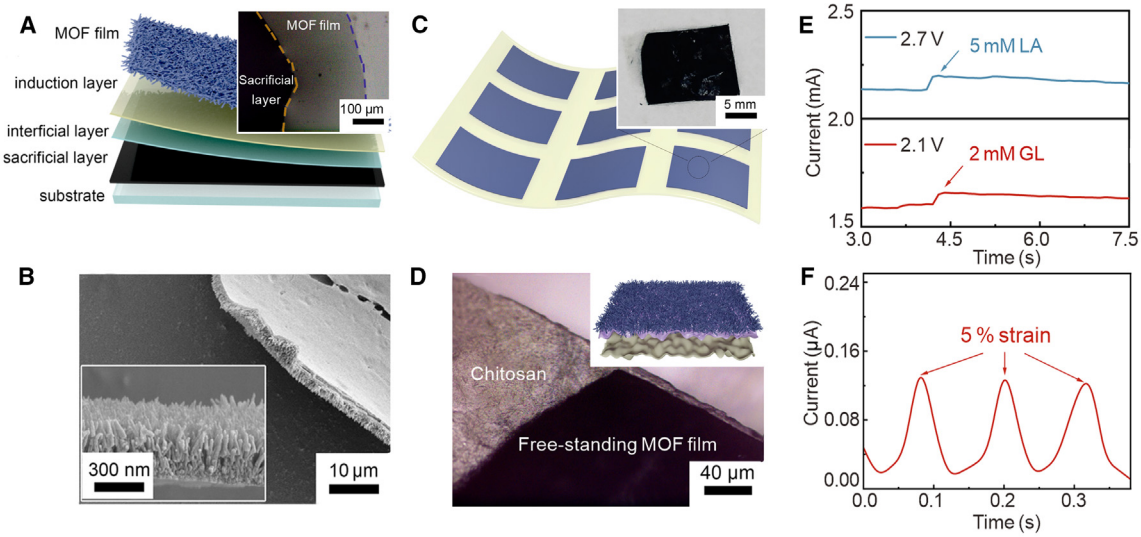

Figure 5. Fabrication and characterization of transferred MOF e-skin array

(A) Fabrication process of the free-standing MOF film. Inset is an optical microscopy image of the free-standing Cu-HHTP film.

(B) SEM image of the free-standing Cu-HHTP film. Inset is SEM image with larger magnification.

(C) Schematic of MOF e-skin array. Inset is photograph of a single transferred MOF e-skin on chitosan film.

(D) Optical microscopy image of single transferred MOF e-skin. Inset is the schematic of the structure of transferred e-skin.

(E) I-t curve of transferred MOF e-skin with the addition of 5 mM GL in 0.1 M PBS at a potential of 2.1 V (red line) and I-t curve of transferred MOF e-skin with the addition of 5 mM LA in 0.1 M PBS at a potential of 2.7 V (blue line).

(F) I-t curve of transferred MOF e-skin with 5% strain applied three times.

transferred MOF e-skin to a 5% strain three times results in stable and reproducible current responses, further highlighting its multi-functional sensing capabilities (Figure 5F).

Conclusions and outlook

This work presents an approach for developing a multi-functional MOF e-skin by utilizing ALD-assisted assembly to grow dense and uniform Cu-HHTP film on chitosan film. The fabricated MOF e-skin demonstrates multi-functional sensing capabilities due to its composite structure. It can independently detect biomolecules (e.g., GL and LA) and various motion signals (e.g., micro-expression, human movement, and ECG signals), and the sensing mechanisms are investigated separately with the help of theoretical calculation. The device showcases rapid response, high repeatability, and remarkable sensitivity across both biomolecular and mechanical sensing modes. By leveraging the transformer neural network, the MOF e-skin can isolate the individual I-t curves for responses from biomolecule and motion and identify different micro-expressions by analyzing the output current. We developed a releasing and transferring process that can be used to fabricate the sensor array with the capability to detect a broader spectrum of objects with increased accuracy in the future.

Enhancing the scalability of the e-skin for mass production and incorporating self-healing and adaptive materials could bring this technology closer to becoming a ubiquitous tool in both consumer and clinical settings. With advanced machine-learning models, the MOF ekin could evolve into an intelligent system capable of autonomously analyzing complex physiological data and providing real-time feedback, elevating healthcare and advancing human interaction technologies.

METHODS

Materials

Shells of Chinese hairy crabs, portunid crabs, were used as the starting material in this study. $Cu(CH_3COO)_2 \cdot H_2O$ ($\geq$97%), HHTP ($\geq$97%), dopamine hydrochloride ($\geq$97%), ascorbic acid ($\geq$99.99%), Nafion (5 wt. %), D(+)-glucose monohydrate (AR, $\geq$99.7%), NaOH (AR, $\geq$99.7%), NaCl (AR, $\geq$99.7%), potassium ferricyanide ($K_3[Fe(CN)_6]$, AR, $\geq$99%) and KCl (AR, $\geq$99.7%) were purchased from Aladdin (Shanghai, China). Sinopharm Chemicals provided 2-methoxyethanol (AR, $\geq$99.5%), zinc acetate dihydrate ($Zn(CH_3COO)_2 \cdot 2H_2O$, AR, $\geq$99.7%), and LA (AR, $\geq$99.7%). Titan supplied methanol (AR, $\geq$99.5%), N, N-dimethylformamide (DMF, AR, $\geq$99.5%), and ethanol (AR, $\geq$99.7%). Sigma-Aldrich provided PEDOT/PSS (1.3 wt. % dispersion in H_2O, conductive grade) and methylimidazole (MI, AR, $\geq$99.7%). Sigma-Aldrich supplied polyethylene (PE) film, polyimide (PI) film, PDMS film, and glass slides. Dulbecco's modified Eagle's medium (DMEM) (calcein-acetoxymethyl ester, AR, $\geq$99%) was bought from Corning. Penicillin (100×) and streptomycin were bought from Beyotime, China. Fetal bovine serum (AR, $\geq$99%) was bought from GIBCO, Australia. The Millipore system was used to purify the de-ionized (DI) water for all experiments. The cell viability of human oral keratinocyte (HOK) cells and CCK-8 assay kit were measured using calcein-AM/propidium iodide (Beyotime, China).

Preparation of the self-locking chitosan film

The crab shells were subjected to an ethanol and water wash. Subsequently, the shells were treated with 1 M HCl at room

Please cite this article in press as: Ke et al., Deep-learning-enhanced metal-organic framework e-skin for health monitoring, Device (2024), https://doi.org/10.1016/j.device.2024.100650

temperature for 24 h to remove any residual calcium minerals. The shells were then rinsed and treated with 5 wt % NaOH at room temperature for 12 h to remove any remaining protein. This step was repeated twice. The pigments were then extracted from the crab shell chitin by using ethanol at room temperature for 12 h. The purified chitin was then immersed in a dilute acetic acid solution (pH $\approx$ 3) for 12 h to facilitate fibrillation of the chitin fibrils. The mixture of crab-shell chitin and acetic acid solution (0.8 wt. % solid content) was blended at 15,000 rpm for several minutes using a high-speed blender to produce a uniform chitin-nanofiber slurry. This slurry was then diluted with distilled water to a concentration of 0.1 wt % and filtered under vacuum using a nylon-membrane filter with a 0.45-μm pore size. The resulting wet film was prepressed at 50°C under 3 MPa for 6 h to strengthen the fiber networks. This was followed by treatment with a concentrated NaOH solution (50 wt. %) at 90°C for 12 h to promote interdigitation. Then, the film was washed several times with DI water and cut into a square shape with scissors. Finally, the film was rinsed and hot-pressed at 50°C under 3 MPa for 12 h to obtain the final water-resistant film.

ALD-assisted deposition of ZnO nanomembrane

ZnO nanomembrane was prepared by ALD on chitosan film. The preparation process was performed at a temperature of 150°C in a custom-designed reactor, and diethylzinc (DEZ) and DI water were utilized as the precursors. The ALD cycle is composed of a DEZ pulse (70 ms), waiting time (2 s), N_2 purge (30 s), DI-water pulse (50 ms), waiting time (2 s), and N_2 purge (30 s). In the current study, the ZnO nanomembrane with 300 ALD cycles (~50 nm) was deposited.

Fabrication of MOF e-skin

A defined mixture of 32.4 mg of HHTP, 10.5 mg of $Cu(CH_3COO)_2 \cdot H_2O$, and 20 mL of methanol was introduced into a 50-mL glass vial, which was then properly sealed. Subsequently, an ALD-ZnO nanomembrane-coated chitosan film was carefully placed within the same vial. The vial was heated to a temperature of 65°C for a period of 24 h. Upon the vial's completion of the heating process and subsequent cooling to room temperature, the samples were carefully collected and washed with a moderate amount of ethanol. For sensor device, Au patterns (50 nm) deposited by E-beam evaporation with shadow mask were used as electrodes.

Synthesis of the MOF powder

MOF powder was prepared for subsequent comparison. A defined mixture of 32.4 mg of HHTP, 10.5 mg of $Cu(CH_3COO)_2 \cdot H_2O$, and 20 mL of methanol was introduced into a 50-mL glass vial, which was then properly sealed. The vial was heated to a temperature of 65°C for a period of 12 h. Upon the vial's completion of the heating process and subsequent cooling to room temperature. The product was centrifuged, followed by three cycles of ethanol washing, prior to being subjected to vacuum drying at 60°C for a duration of 24 h.

Fabrication of free-standing MOF film and transferred device

A uniform PEDOT/PSS layer with a thickness of approximately 10 μm is spun-coated onto the slide substrate as a sacrificial layer, followed by a 6-h solidification at 90°C. Al_2O_3 nanomembrane was then deposited by ALD on the sacrificial layer. The preparation process was performed at a temperature of 120°C in a custom-designed reactor, and trimethylaluminium (TMA) and DI water were utilized as the precursors. The ALD cycle is composed of a TMA pulse (60 ms), a waiting period (2 s), an N_2 purge (30 s), a DI-water pulse (60 ms), a waiting period (2 s), and an N_2 purge (30 s). In this work, the Al_2O_3 nanomembrane was deposited on substrates with 200 ALD cycles. The following step is the deposition of ZnO nanomembrane with 300 ALD cycles. Then, the sample was carefully placed within the same vial. The vial was heated to a temperature of 65°C for a period of 12 h. Upon the completion of the heating and subsequent cooling to room temperature, the sample was carefully collected and washed with a moderate amount of ethanol. Finally, the free-standing Cu-HHTP film was peeled off by using DI water. As a substrate, chitosan film was prepared separately. Au patterns (50 nm) were deposited by sputtering on chitosan film with shadow mask and used as electrodes. The free-standing Cu-HHTP film was then transferred onto the chitosan film with electrodes. The device was pasted on the surface of human skin and wires were used for signal output.

Structural characterizations

The sample morphologies were characterized by using field-emission SEM (Gemini 560, Zeiss). More details of structural characterizations can be found in Note S7.

Electrochemical characterizations

The electrochemical activity measurements were conducted using solutions prepared with 0.1 M PBS, pH 7.2. The experiments to assess the electrochemical properties were conducted by using a Zennium X instrument (Zahner Instrument, Germany), employing a three-electrode configuration. An Ag/AgCl electrode (immersed in saturated KCl solution) served as the reference electrode, and a graphite rod served as the counter electrode. The test samples were affixed to the platinum electrode clamp using Nafion to enhance the sample-clamp connection.

RESOURCE AVAILABILITY

Lead contact

Further information and requests for resources and materials should be directed to and will be fulfilled by the lead contact, Gaoshan Huang (gshuang@fudan.edu.cn).

Materials availability

This study did not generate new and unique reagents.

Data and code availability

All data and original code required to evaluate the conclusions in this article are provided within the article and supplemental information. The output data of the sensor within the datasets are provided as a demo datasets in Data S1 (Data S1.zip). The corresponding Python coding environment setup information is in Data S2 (Data S2.zip). The transformer model, along with the code for model training and testing, is included in Data S3 (Data S3. zip) and Data S4 (Data S4.zip), respectively. A README.md file is provided in Data S5.zip to assist users in understanding the background, functionalities, dependencies, and detailed instructions on installation, usage, and execution of the code.

ACKNOWLEDGMENTS

This work is supported by the National Key Technologies R&D Program of China (2021YFA0715302), the National Natural Science Foundation of China (52203328 and 62375054), the Science and Technology Commission of Shanghai Municipality (22ZR1405000 and 21142200200), the Fundamental Research Funds for the Central Universities (2232023A-10), and the Major/Key Program of State Key Laboratory for Modification of Chemical Fibers and Polymer Materials (23M1060280).

AUTHOR CONTRIBUTIONS

Z. Zhao, G.H., and Y.M. conceived the project and designed experiments. X.K. prepared e-skin and characterized the sensor with assistance from T.S. and W.X. Yifei Duan., Yifan Duan, and X.G. assisted X.K. with transformer neural network and analyzed the data. C.Y. and Z. Zhang assisted X.K. with theoretical analysis. X.K, Z. Zhao, and G.H. co-wrote the paper. Y.M., X.L., and G.H. discussed the results and commented on the manuscript.

DECLARATION OF INTERESTS

The authors declare no competing interests.

SUPPLEMENTAL INFORMATION

Supplemental information can be found online at https://doi.org/10.1016/j.device.2024.100650.

Received: July 15, 2024
Revised: July 16, 2024
Accepted: November 28, 2024
Published: January 7, 2025

REFERENCES

1. Peng, X., Dong, K., Ye, C., Jiang, Y., Zhai, S., Cheng, R., Liu, D., Gao, X., Wang, J., and Wang, Z.L. (2020). A breathable, biodegradable, antibacterial, and self-powered electronic skin based on all-nanofiber triboelectric nanogenerators. Sci. Adv. *6*, eaba9624. https://doi.org/10.1126/sciadv.aba9624.
2. Tee, B.C.-K., Chortos, A., Berndt, A., Nguyen, A.K., Tom, A., McGuire, A., Lin, Z.C., Tien, K., Bae, W.-G., Wang, H., et al. (2015). A skin-inspired organic digital mechanoreceptor. Science *350*, 313–316. https://doi.org/10.1126/science.aaa9306.
3. Jiaqi, T., Ming, W., Wenlong, L., Jiangtao, S., Yanzhen, L., Zhisheng, L., Haicheng, L., Xue, F., and Xiaodong, C. (2023). Electronic skins with multimodal sensing and perception. Soft Sci. *3*, 25. https://www.oaepublish.com/articles/ss.2023.15.
4. Luo, Y., Abidian, M.R., Ahn, J.-H., Akinwande, D., Andrews, A.M., Antonietti, M., Bao, Z., Berggren, M., Berkey, C.A., Bettinger, C.J., et al. (2023). Technology roadmap for flexible sensors. ACS Nano *17*, 5211–5295. https://doi.org/10.1021/acsnano.2c12606.
5. Zhuang, Q., Yao, K., Zhang, C., Song, X., Zhou, J., Zhang, Y., Huang, Q., Zhou, Y., Yu, X., and Zheng, Z. (2024). Permeable, three-dimensional integrated electronic skins with stretchable hybrid liquid metal solders. Nat. Electron. *7*, 598–609. https://doi.org/10.1038/s41928-024-01189-x.
6. Liu, Z., Hu, X., Bo, R., Yang, Y., Cheng, X., Pang, W., Liu, Q., Wang, Y., Wang, S., Xu, S., et al. (2024). A three-dimensionally architected electronic skin mimicking human mechanosensation. Science *384*, 987–994. https://doi.org/10.1126/science.adk5556.
7. Yang, X., Yi, J., Wang, T., Feng, Y., Wang, J., Yu, J., Zhang, F., Jiang, Z., Lv, Z., Li, H., et al. (2022). Wet-adhesive on-skin sensors based on metal–organic frameworks for wireless monitoring of metabolites in sweat. Adv. Mater. *34*, 2201768. https://doi.org/10.1002/adma.202201768.
8. Zhong, B., Jiang, K., Wang, L., and Shen, G. (2022). Wearable sweat loss measuring devices: from the role of sweat loss to advanced mechanisms and designs. Adv. Sci. *9*, 2103257. https://doi.org/10.1002/advs.202103257.
9. Su, J., Zhang, H., Li, H., He, K., Tu, J., Zhang, F., Liu, Z., Lv, Z., Cui, Z., Li, Y., et al. (2024). Skin-inspired multi-modal mechanoreceptors for dynamic haptic exploration. Adv. Mater. *36*, 2311549. https://doi.org/10.1002/adma.202311549.
10. Chen, H., Xiang, Y., Cai, R., Zhang, L., Zhang, Y., and Zhou, N. (2021). An ultrasensitive biosensor for dual-specific DNA based on deposition of polyaniline on a self-assembled multi-functional DNA hexahedral-nanostructure. Biosens. Bioelectron. *179*, 113066. https://doi.org/10.1016/j.bios.2021.113066.
11. Hu, X., Khanzada, S., Klütsch, D., Calegari, F., and Amin, H. (2022). Implementation of biohybrid olfactory bulb on a high-density CMOS-chip to reveal large-scale spatiotemporal circuit information. Biosens. Bioelectron. *198*, 113834. https://doi.org/10.1016/j.bios.2021.113834.
12. Liu, Y., Li, X., Yang, H., Zhang, P., Wang, P., Sun, Y., Yang, F., Liu, W., Li, Y., Tian, Y., et al. (2023). Skin-interfaced superhydrophobic insensible sweat sensors for evaluating body thermoregulation and skin barrier functions. ACS Nano *17*, 5588–5599. https://doi.org/10.1021/acsnano.2c11267.
13. Bi, Y., Sun, M., Wang, J., Zhu, Z., Bai, J., Emran, M.Y., Kotb, A., Bo, X., and Zhou, M. (2023). Universal fully integrated wearable sensor arrays for the multiple electrolyte and metabolite monitoring in raw sweat, saliva, or urine. Anal. Chem. *95*, 6690–6699. https://doi.org/10.1021/acs.analchem.3c00361.
14. Gao, W., Emaminejad, S., Nyein, H.Y.Y., Challa, S., Chen, K., Peck, A., Fahad, H.M., Ota, H., Shiraki, H., Kiriya, D., et al. (2016). Fully integrated wearable sensor arrays for multiplexed in situ perspiration analysis. Nature *529*, 509–514. https://doi.org/10.1038/nature16521.
15. Wu, Y., Li, Y., Jin, K., Zhang, L., Li, J., Liu, Y., Du, G., Lv, X., Chen, J., Ledesma-Amaro, R., and Liu, L. (2023). CRISPR–dCas12a-mediated genetic circuit cascades for multiplexed pathway optimization. Nat. Chem. Biol. *19*, 367–377. https://doi.org/10.1038/s41589-022-01230-0.
16. Veenuttranon, K., Kaewpradub, K., and Jeerapan, I. (2023). Screen-printable functional nanomaterials for flexible and wearable single-enzyme-based energy-harvesting and self-powered biosensing devices. Nano-Micro Lett. *15*, 85. https://doi.org/10.1007/s40820-023-01045-1.
17. Bariya, M., Nyein, H.Y.Y., and Javey, A. (2018). Wearable sweat sensors. Nat. Electron. *1*, 160–171. https://www.nature.com/articles/s41928-018-0043-y.
18. Wang, J., Wang, C., Cai, P., Luo, Y., Cui, Z., Loh, X.J., and Chen, X. (2021). Artificial sense technology: emulating and extending biological senses. ACS Nano *15*, 18671–18678. https://doi.org/10.1021/acsnano.1c10313.
19. Lv, Z., Wang, C., Wan, C., Wang, R., Dai, X., Wei, J., Xia, H., Li, W., Zhang, W., Cao, S., et al. (2022). Strain-driven auto-detachable patterning of flexible electrodes. Adv. Mater. *34*, 2202877. https://doi.org/10.1002/adma.202202877.
20. Li, Y., Wang, R., Wang, G.-E., Feng, S., Shi, W., Cheng, Y., Shi, L., Fu, K., and Sun, J. (2022). Mutually noninterfering flexible pressure–temperature dual-modal sensors based on conductive Metal–Organic Framework for electronic skin. ACS Nano *16*, 473–484. https://doi.org/10.1021/acsnano.1c07388.
21. Xu, C., Song, Y., Sempionatto, J.R., Solomon, S.A., Yu, Y., Nyein, H.Y.Y., Tay, R.Y., Li, J., Heng, W., Min, J., et al. (2024). A physicochemical-sensing electronic skin for stress response monitoring. Nat. Electron. *7*, 168–179. https://doi.org/10.1038/s41928-023-01116-6.
22. Ates, H.C., Nguyen, P.Q., Gonzalez-Macia, L., Morales-Narváez, E., Güder, F., Collins, J.J., and Dincer, C. (2022). End-to-end design of wearable sensors. Nat. Rev. Mater. *7*, 887–907. https://doi.org/10.1038/s41578-022-00460-x.

23. Liu, Z., Zheng, Y., Jin, L., Chen, K., Zhai, H., Huang, Q., Chen, Z., Yi, Y., Umar, M., Xu, L., et al. (2021). Highly breathable and stretchable strain sensors with insensitive response to pressure and bending. Adv. Funct. Mater. *31*, 2007622. https://doi.org/10.1002/adfm.202007622.

24. Kubo, M., Sugahara, T., and Shimada, M. (2021). Facile fabrication of HKUST-1 thin films and free-standing MWCNT/HKUST-1 film using a spray-assisted method. Microporous Mesoporous Mater. *312*, 110771. https://doi.org/10.1016/j.micromeso.2020.110771.

25. Ling, W., Liew, G., Li, Y., Hao, Y., Pan, H., Wang, H., Ning, B., Xu, H., and Huang, X. (2018). Materials and techniques for implantable nutrient sensing using flexible sensors integrated with metal–organic frameworks. Adv. Mater. *30*, 1800917. https://doi.org/10.1002/adma.201800917.

26. Zhang, B., Dai, X., Wei, N., Cui, X., Fan, F., Zhang, J., Zhang, D., Meng, F., Qi, W., and Fu, Y. (2024). Fabrication of oriented mof-based mixed matrix membrane via ion-induced synchronous synthesis. Small *20*, 2305688. https://doi.org/10.1002/smll.202305688.

27. Yang, H., Zhao, Y., Guo, Y., Wu, B., Ying, Y., Sofer, Z., and Wang, S. (2024). Surfactant-mediated crystalline structure evolution enabling the ultrafast green synthesis of bismuth-mof in aqueous condition. Small *20*, 2307484. https://doi.org/10.1002/smll.202307484.

28. Shahrokhian, S., Khaki Sanati, E., and Hosseini, H. (2018). Direct growth of metal-organic frameworks thin film arrays on glassy carbon electrode based on rapid conversion step mediated by copper clusters and hydroxide nanotubes for fabrication of a high performance non-enzymatic glucose sensing platform. Biosens. Bioelectron. *112*, 100–107. https://doi.org/10.1016/j.bios.2018.04.039.

29. Zhao, Z., Ke, X., Huang, J., Zhang, Z., Wu, Y., Huang, G., Tan, J., Liu, X., Mei, Y., and Chu, J. (2024). Design and synthesis of transferrable macro-sized continuous free-standing metal-organic framework films for biosensor device. Adv. Sci. *11*, 2310189. https://doi.org/10.1002/advs.202310189.

30. Ke, X., Zhao, Z., Huang, J., Liu, C., Huang, G., Tan, J., Zhu, H., Xiao, Z., Liu, X., Mei, Y., and Chu, J. (2023). Growth control of Metal–Organic Framework films on marine biological carbon and their potential-dependent dopamine sensing. ACS Appl. Mater. Interfaces *15*, 12005–12016. https://doi.org/10.1021/acsami.2c20517.

31. Zhao, Z., Kong, Y., Huang, G., Liu, C., You, C., Xiao, Z., Zhu, H., Tan, J., Xu, B., Cui, J., et al. (2022). Area-selective and precise assembly of metal organic framework particles by atomic layer deposition induction and its application for ultra-sensitive dopamine sensor. Nano Today *42*, 101347. https://doi.org/10.1016/j.nantod.2021.101347.

32. Lu, Z., Ke, X., Zhao, Z., Huang, J., Liu, C., Wang, J., Xu, R., Mei, Y., and Huang, G. (2024). Fabrication of NiCo bimetallic MOF films on 3D Foam with assistance of atomic layer deposition for non-invasive lactic acid sensing. ACS Appl. Mater. Interfaces *16*, 14218–14228. https://doi.org/10.1021/acsami.4c01573.

33. Nie, P., Wang, R., Xu, X., Cheng, Y., Wang, X., Shi, L., and Sun, J. (2017). High-performance piezoresistive electronic skin with bionic hierarchical microstructure and microcracks. ACS Appl. Mater. Interfaces *9*, 14911–14919. https://doi.org/10.1021/acsami.7b01979.

34. Wang, D., Ostresh, S., Streater, D., He, P., Nyakuchena, J., Ma, Q., Zhang, X., Neu, J., Brudvig, G.W., and Huang, J. (2023). Dominant role of hole transport pathway in achieving record high photoconductivity in two-dimensional metal–organic frameworks. Angew. Chem. Int. Ed. *62*, e202309505. https://doi.org/10.1002/anie.202309505.

35. Lin, L., Zhang, Q., Ni, Y., Shang, L., Zhang, X., Yan, Z., Zhao, Q., and Chen, J. (2022). Rational design and synthesis of two-dimensional conjugated metal-organic polymers for electrocatalysis applications. Chem *8*, 1822–1854. https://doi.org/10.1016/j.chempr.2022.03.027.

36. Zhao, Z., Ke, X., Huang, J., Zhang, Z., Wu, Y., Huang, G., Tan, J., Liu, X., Mei, Y., and Chu, J. (2024). Design and synthesis of transferrable macro-sized continuous free-standing Metal-Organic Framework films for biosensor device. Adv. Sci. *11*, 2310189. https://doi.org/10.1002/advs.202310189.

37. Vaswani, A., Shazeer, N.M., Parmar, N., Uszkoreit, J., Jones, L., Gomez, A.N., Kaiser, L., and Polosukhin, I. (2017). Attention is all you need. Preprint at arxiv. https://arxiv.org/abs/1706.03762.

38. Zhu, M., Chai, Y., Yuan, R., Zu, B., and Yuan, Y. (2021). Dual catalytic hairpin assembly and enzyme cascade catalysis amplification based sensitive dual-mode biosensor with significantly enhanced opposite signal readout. Sens. Actuators, B. *48*, 130676. https://doi.org/10.1016/j.snb.2021.130676.

39. Zhao, Z., Kong, Y., Lin, X., Liu, C., Liu, J., He, Y., Yang, L., Huang, G., and Mei, Y. (2020). Oxide nanomembrane induced assembly of a functional smart fiber composite with nanoporosity for an ultra-sensitive flexible glucose sensor. J. Mater. Chem. A *8*, 26119–26129. https://doi.org/10.1039/D0TA09211H.

40. Chen, X., Liu, D., Cao, G., Tang, Y., and Wu, C. (2019). In situ synthesis of a sandwich-like graphene@ZIF-67 heterostructure for highly sensitive nonenzymatic glucose sensing in human serums. ACS Appl. Mater. Interfaces *11*, 9374–9384. https://doi.org/10.1021/acsami.8b22478.

41. Zhang, X., Zhang, Y., Guo, W., Wan, K., Zhang, T., Arbiol, J., Zhao, Y.-Q., Xu, C.-L., Xu, M., and Fransaer, J. (2020). A yolk–albumen–shell structure of mixed Ni–Co oxide with an ultrathin carbon shell for high-sensitivity glucose sensors. Mater. Adv. *1*, 908–917. https://doi.org/10.1039/D0MA00230E.

42. Li, W., Lv, S., Wang, Y., Zhang, L., and Cui, X. (2019). Nanoporous gold induced vertically standing 2D NiCo bimetal-organic framework nanosheets for non-enzymatic glucose biosensing. Sens. Actuators, B *281*, 652–658. https://doi.org/10.1016/j.snb.2018.10.150.

43. Wu, L., Lu, Z., and Ye, J. (2019). Enzyme-free glucose sensor based on layer-by-layer electrodeposition of multilayer films of multi-walled carbon nanotubes and Cu-based metal framework modified glassy carbon electrode. Biosens. Bioelectron. *135*, 45–49. https://doi.org/10.1016/j.bios.2019.03.064.

44. Chen, C., Xiong, D., Gu, M., Lu, C., Yi, F.-Y., and Ma, X. (2020). MOF-Derived bimetallic CoFe-PBA composites as highly selective and sensitive electrochemical sensors for hydrogen peroxide and nonenzymatic glucose in human serum. ACS Appl. Mater. Interfaces *12*, 35365–35374. https://doi.org/10.1021/acsami.0c09689.

45. Cheng, S., Gao, X., DelaCruz, S., Chen, C., Tang, Z., Shi, T., Carraro, C., and Maboudian, R. (2019). In situ formation of metal–organic framework derived CuO polyhedrons on carbon cloth for highly sensitive non-enzymatic glucose sensing. J. Mater. Chem. B *7*, 4990–4996. https://doi.org/10.1039/C9TB01166H.

46. Dosovitskiy, A., Beyer, L., Kolesnikov, A., Weissenborn, D., Zhai, X., Unterthiner, T., Dehghani, M., Minderer, M., Heigold, G., Gelly, S., et al. (2020). An image is worth 16x16 words. Transformers for image recognition at scale Preprint at. arxiv. https://arxiv.org/abs/2010.11929.